

Pt–Ru and Pt–Ru–P/Carbon Nanocomposites: Synthesis, Characterization, and Unexpected Performance as Direct Methanol Fuel Cell (DMFC) Anode Catalysts

William D. King,[†] James D. Corn,[†] Oliver J. Murphy,[‡] Deborah L. Boxall,[†] Edward A. Kenik,[#] Krzysztof C. Kwiatkowski,[†] Stuart R. Stock,[§] and C. M. Lukehart^{*,†}

Department of Chemistry, Vanderbilt University, Nashville, Tennessee 37235, Lynntech, Inc., 7610 Eastmark Drive, Suite 105, College Station, Texas 77840, Oak Ridge National Laboratory, Oak Ridge, Tennessee 37831, and the School of Materials Science and Engineering, Georgia Institute of Technology, Atlanta, Georgia 30332

Received: January 14, 2003

Six Pt–Ru/carbon nanocomposites have been prepared, using five different Pt,Ru-bimetallic precursors as sources of metal. Nanocomposites prepared from precursors lacking phosphorus contain Pt–Ru nanocrystals that are highly dispersed on the carbon support, as expected. However, nanocomposites prepared from precursors possessing phosphorus contain a mixture of face-centered-cubic Pt–Ru alloy nanocrystals and primitive-cubic nanocrystals of an interstitial ternary metal phosphide phase identified as PtRuP₂. Nanocomposites containing substantial amounts of nano-PtRuP₂ perform as well as a commercial Pt–Ru/carbon nanocomposite in the role of an anode catalyst in direct methanol fuel cells. Although the exclusion of metal phosphide phases in Pt–Ru nanocomposite syntheses is best achieved by eliminating all sources of phosphorus, the presence of PtRuP₂ in such nanocomposites does not poison methanol electrooxidation. Investigation of the synthesis and electrocatalytic reactivity of pure PtRuE_x (where E denotes a main-group heteroelement) phases is suggested.

Introduction

In direct methanol fuel cells (DMFCs), aqueous methanol is electrooxidized to produce CO₂ and electrical current.¹ Electrocatalysts having higher activity for methanol oxidation are critically needed to achieve enhanced DMFC performance. The search for active methanol oxidation catalysts has involved the variation of both catalyst preparation strategy and catalyst composition.^{1a}

Mixed-metal catalysts containing platinum are currently favored for methanol oxidation.¹ Platinum activates the C–H bonds of methanol, producing a Pt–CO and other surface species, whereas an oxophilic metal activates water to accelerate the oxidation of surface-adsorbed CO to CO₂. Although combinatorial studies indicate that ternary and quaternary alloy compositions can possess high activity as DMFC anode catalysts,² there remains much interest in improving the activity of more-established binary catalysts containing platinum and ruthenium. Unsupported Pt–Ru colloids and Pt–Ru/carbon nanocomposites have been prepared by a variety of chemical methods, including solution-phase reduction of metal ions and thermal decomposition of either single-source or dual-source molecular precursors.^{1,3} Carbonaceous support materials have included carbon powder, carbon blacks, desulfurized carbon blacks, and fullerene soot.^{3d} DMFC testing data indicate high performance when either unsupported or supported Pt–Ru catalysts are used, depending on anode catalyst composition and particle size.^{3g,4}

We have recently prepared Pt–Ru/carbon nanocomposites having an alloy composition of ca. Pt₁Ru₁ using the (1:1)-Pt–Ru bimetallic precursor (η -C₂H₄)(Cl)Pt(μ -Cl)₂Ru(Cl)(η^3 : η^3 -2,7-dimethyloctadienediyl) (**1a**) as a source of metal.^{5,6} When tested as an anode catalyst in a DMFC, the resulting cell performance of Pt–Ru/Vulcan carbon powder nanocomposites prepared by this method is essentially equivalent to that determined under identical conditions for a commercial, unsupported Pt₁Ru₁ colloidal catalyst.

Such promising results prompted greater investigation of the use of (1:1)-Pt,Ru bimetallic complexes as precursors to Pt–Ru/carbon nanocomposites for potential use as DMFC anode catalysts.⁷ We now report the preparation and characterization of six Pt–Ru/Vulcan carbon nanocomposites using five different (1:1)-Pt,Ru bimetallic complexes as sources of metal, along with the testing results for two such nanocomposites as DMFC anode catalysts. Included as precursors are three neutral, organometallic complexes (**1a**, (Ph₃P)(Cl)Pt(μ -Cl)₂Ru(Cl)(η^3 : η^3 -2,7-dimethyloctadienediyl), and (Et₃P)(Cl)Pt(μ -Cl)₂Ru(Cl)(η^3 : η^3 -2,7-dimethyloctadienediyl)) and two ionic coordination complexes ([(2,2'-bipyridine)₂Ru(μ -2,2'-bipyrimidine)PtCl₂][BF₄]₂ and [(2,2'-bipyridine)₂Ru(μ -2,2'-bipyrimidine)PtCl₂][PF₆]₂). All these precursors are noncluster, bimetallic complexes in which bridging ligands coordinate to both metals without involving direct Pt–Ru covalent bonding.

Upon subjecting precursor/carbon composites to conventional tube furnace thermal treatments under inert or reactive gaseous atmospheres, each sample is successfully transformed to a Pt–Ru alloy/carbon nanocomposite, as expected.^{5–7} However, a second metal-containing phase, identified as the interstitial ternary metal phosphide PtRuP₂, is commonly present in nanocomposites prepared from precursors containing phosphorus. DMFC performance data indicate that the presence of

Author to whom correspondence should be addressed. E-mail: charles.m.lukehart@vanderbilt.edu.

[†] Vanderbilt University.

[‡] Lynntech, Inc.

[#] Oak Ridge National Laboratory.

[§] Georgia Institute of Technology.

significant amounts of this ternary metal phosphide phase does not significantly reduce the performance of such catalysts, relative to the performance of commercial Pt–Ru/C electrocatalysts. In contrast to the known poisoning effect of surface-bound sulfur,⁸ the presence of phosphorus as an interstitial species does not appear to inhibit methanol electrooxidation. This unexpected observation raises the interesting possibility that ternary phases of composition PtRuE_x (where E is a main-group heteroelement) might possibly exhibit enhanced performance as DMFC anode catalysts. We speculate that the intentional incorporation of main-group heteroelements as interstitial species in Pt–Ru alloys might permit compositional tuning of the electrocatalytic reactivity of these important catalysts.

Experimental Section

General Methods. All gaseous reagents were procured from Aire Liquide Gas. Nitrogen gas used in the following reactions was prepurified and passed through a drying column prior to use. All solvents were reagent grade and were distilled under dry nitrogen prior to use. Dimethyl sulfoxide (DMSO) was purchased from Fisher Chemical Co. Triphenylphosphine (PPh₃) was purchased from Pressure Chemical Company. The reagents K₂PtCl₄, RuCl₂(2,2′-bipyridine)₂·2H₂O, Pt₂Cl₄(C₂H₄)₂, PET₃, and RuCl₃·*n*H₂O were purchased from Strem Chemical Company, Inc. 2,2′-Bipyrimidine (C₈H₆N₄, bpm) and NaBF₄ were purchased, respectively, from Lancaster Chemical Company, Inc., and Aldrich Chemical Co., Inc. Pt₂Cl₂(μ₂-Cl)₂(PPh₃)₂,⁹ Pt₂Cl₂(μ₂-Cl)₂(PET₃)₂,¹⁰ *cis*-(DMSO)PtCl₂,¹¹ Ru₂Cl₂(μ₂-Cl)₂(η³:η³-2,7-dimethyloctadienediyl)₂,¹² [Ru(bpy)₂(bpm)][PF₆]₂,¹³ and (η-C₂H₄)(Cl)Pt(μ-Cl)₂Ru(Cl)(η³:η³-2,7-dimethyloctadienediyl) (**1a**)⁵ were prepared following literature procedures. In this paper, 2,2′-bipyridine (C₁₀H₈N₂) will be denoted as bpy and η³:η³-2,7-dimethyloctadienediyl will be denoted as η³:η³-C₁₀H₁₆.

Nuclear magnetic resonance (NMR) spectra were obtained on a Bruker model AC300 Fourier transform spectrometer. ¹H and ¹³C NMR chemical shifts (δ) are referenced to tetramethylsilane, using, respectively, the residual proton resonance and the carbon resonance of the deuterated solvent as an internal standard. ³¹P NMR chemical shifts (δ) are referenced to H₃-PO₄. Elemental analyses were performed by Galbraith Laboratories, Inc. (Knoxville, TN) or VHG Labs, Inc. (Manchester, NH).

Nanocomposite materials were characterized using a Philips model CM20T transmission electron microscope (TEM), operating at 200 kV, which was equipped with an energy-dispersive X-ray analysis (EDAX) X-ray detector. Samples were prepared for analysis by allowing the solvent to evaporate from a methylene chloride suspension of the powdered material onto a TEM grid (3-mm diameter copper grid coated with amorphous holey carbon, from Ted Pella, Inc.). The samples were analyzed by standard bright-field (BF) imaging for particle-size distribution, selected-area electron diffraction (SAD) for their crystal structures, and X-ray energy-dispersive spectroscopy (EDS) for semiquantitative determination of the chemical composition.

Single-particle high-spatial-resolution energy-dispersive spectroscopy (HR-EDS) was used to examine variations in the particle composition, using a Philips model CM200FEG 200 kV TEM equipped with an Oxford light-element EDS detector and an EMISPEC Vision data acquisition system at the SHaRE Collaboration Research Center in the Metals and Ceramics Division of Oak Ridge National Laboratory. The HR-EDS data were collected using a tilt angle of 15°, an acceleration voltage of 200 kV, a collection time of 20 s, and a 1.4-nm diameter

probe in the stopped-scan mode. Integrated intensities from the Pt Lα₁ and the Ru Kα_{1,2} lines were used for quantification, because they were not overlapped by any other X-ray emissions. The X-ray emission cross sections that were appropriate for the instrumental geometry and the spurious contributions from the Vulcan carbon support were obtained by measuring the Pt and Ru emission intensities for 100 s from several 1-μm² areas of a sample with a known bulk chemical composition, as determined from commercial chemical elemental analysis. Ru emission intensities were corrected for any loss of ruthenium mass, using a reported computational model.⁵

X-ray diffraction (XRD) scans were obtained either using a Scintag X1 Advanced Diffraction System equipped with a copper target, a solid-state Peltier detector, a Buehler HDK high-temperature unit, and a gas delivery system, or using a Philips model PW1800 θ/2θ automated powder diffractometer equipped with a copper target and a post-sample monochromator. Samples analyzed on the Scintag instrument were prepared for XRD analysis by allowing the solvent to evaporate from a pentane suspension of the powdered material onto a silicon (510) zero-background slide, giving a uniform layer with approximate dimensions of 12 mm × 20 mm. This sample area was greater than the area irradiated by the X-ray beam. Prior to peak-width measurements, each diffraction peak was corrected for background scattering and stripped of the Kα₂ portion of the diffracted intensity, using the Scintag DMSNT software package (version 1.30c).¹⁴ The full width at half maximum (fwhm) was determined from peak profiles calculated for each observed peak by the DMSNT software. Crystallite size, *L*, was calculated using Scherrer's equation for peak broadening from size effects only ($L = K\lambda/(\beta \cos \theta_B)$), where *K* is a constant equal to 0.9, λ the wavelength of X-rays used, β the fwhm measured in radians on the 2θ scale, and θ_B the Bragg angle for the measured *hkl* peak.¹⁴

Samples analyzed on the Philips CM20T TEM were prepared by placing a uniform layer of powdered nanocomposite onto double-sided tape that was affixed to the sample holder. The sample area was greater than the ca. 1 cm × 1 cm area irradiated by the X-ray beam. Considerable caution was used to keep the top of the sample surface flat and coplanar with the diffractometer rotation axis.

Preparation of [Bis-(2,2′-bipyridine)-2,2′-bipyrimidineruthenium(II)][BF₄]₂. The complex [Ru(bpy)₂(bpm)][BF₄]₂ was prepared by a modification of procedures for the synthesis of the corresponding PF₆[−] salt.¹³ To a solution of 0.465 g (0.96 mmol) of Ru(bpy)₂Cl₂ in 50 mL of a 2:1 ethanol/water solution was added 0.276 g (1.75 mmol) of 2,2′-bipyrimidine. The resulting suspension was stirred and heated at reflux under a N₂ atmosphere for 2 h. After the reaction solution was cooled to near room temperature, it was added to 50 mL of an aqueous solution containing 1.0 g (9.1 mmol) of NaBF₄. Precipitate formation was induced by solvent evaporation at reduced pressure. The obtained solid residue was dissolved in a minimal volume of 3:2 toluene/acetonitrile solution and was developed on an adsorption alumina column, using the toluene/acetonitrile solution as the eluant. A single orange band was collected, and the solvent was removed by rotoevaporation. The crude product was redissolved in a minimal amount of acetonitrile, flash-precipitated with diethyl ether, and collected by vacuum filtration. The bright orange solid was washed with diethyl ether and dried under reduced pressure at 80 °C to give 0.357 g (0.48 mmol, 50% yield) of the desired product Anal. Calcd for C₂₈H₂₂N₈B₂F₈Ru·3H₂O: C, 42.08; H, 3.56; N, 14.22. Found: C, 41.81; H, 3.41; N, 13.91.

Preparation of [(2,2'-Bipyridine)₂Ru(μ-2,2'-bipyrimidine)-PtCl₂][BF₄]₂, **2a.** The synthesis of [(bpy)₂Ru(μ-bpm)PtCl₂][BF₄]₂ was performed using a modification of a method reported for the synthesis of the ClO₄[−] salt of this compound.¹⁵ A solution of 0.200 g (0.474 mmol) of (DMSO)₂PtCl₂ and 0.353 g (0.474 mmol) of [Ru(bpy)₂(bpm)][BF₄]₂ in 50 mL of deoxygenated methanol was heated at reflux in darkness under a N₂ atmosphere for ca. 12 h. After the solution was cooled, a precipitate formed, which was collected by vacuum filtration, washed with diethyl ether, and dried under reduced pressure near room temperature for 4 h to give 0.443 g of **2a** as a brick-red solid (0.42 mmol, 92.5% yield). Anal. Calcd for C₂₈H₂₂N₈B₂F₈Cl₂-RuPt: C, 33.26; H, 2.19; N, 11.08. Found: C, 33.28; H, 2.23; N, 11.16.

Preparation of Pt(PPh₃)(Cl)(μ₂-Cl)₂Ru(Cl)(η³:η³-C₁₀H₁₆), **3a.** The molecular precursor complex Pt(PPh₃)(Cl)(μ₂-Cl)₂Ru(Cl)(η³:η³-C₁₀H₁₆) was prepared using a modification of the procedures reported for the synthesis of analogous complexes.¹⁶ A solution of 0.718 g (0.680 mmol) of Pt₂Cl₂(μ₂-Cl)₂(PPh₃)₂ and 0.417 g (0.677 mmol) of Ru₂Cl₂(μ₂-Cl)₂(C₁₀H₁₆)₂ in 100 mL of CH₂Cl₂ was stirred at room temperature for ca. 16 h under a N₂ atmosphere. The solvent was removed from the reddish-brown solution at reduced pressure to give a brown powder. Recrystallization of this crude product from acetone/hexane solution at ca. −15 °C gave 0.981 g of **3a** (86% yield, mp 140–146 °C) as a brown solid. ¹H NMR data indicated that a small amount of a second isomer was present in the sample. An isomer having the PPh₃ and C₁₀H₁₆ ligands occupying mutually trans orientations is the major isomer that is usually observed for this type of complex.¹⁶ ¹H NMR [300 MHz, CDCl₃, major isomer]: δ 2.30 (s, CH₂CHC(CH₃)CH₂, 3H), 2.38 (s, CH₂CHC(CH₃)CH₂, 3H), 2.40 (m, CH₂CHC(CH₃)CH₂, 2H), 2.5–2.8 (m, CH₂CHC(CH₃)CH₂, 2H), 4.52 (m, CH₂CHC(CH₃)CH₂, 1H), 4.89 (s, CH₂CHC(CH₃)CH₂, 1H), 4.94 (m, CH₂CHC(CH₃)CH₂, 1H), 5.32 (s, CH₂CHC(CH₃)CH₂, 1H), 5.48 (s, CH₂CHC(CH₃)CH₂, 1H), 5.99 (s, CH₂CHC(CH₃)CH₂, 1H), 7.3–7.8 (m, Ph, 15H). ¹³C NMR [75 MHz, CDCl₃, major isomer]: δ 19.7 and 20.5 (CH₂CHC(CH₃)CH₂), 34.2 and 35.0 (CH₂CHC(CH₃)CH₂), 82.8 and 85.4 (CH₂CHC(CH₃)CH₂), 93.8 and 94.4 (CH₂CHC(CH₃)CH₂), 128.3 (d, Ph_{or}, ²J_{PC} = 12 Hz), 131.4 (s, Ph_{pa}), 134.6 (d, Ph_{me}, ³J_{PC} = 10 Hz). ³¹P NMR [121 MHz, CDCl₃, major isomer]: δ 4.43 (¹J_{PP} = 4079 Hz). Anal. Calcd for C₂₈H₃₁Cl₄-PPtRu: C, 40.20; H, 3.74; P, 3.70. Found: C, 39.75; H, 3.66; P, 3.81.

Preparation of Pt(PEt₃)(Cl)(μ₂-Cl)₂Ru(Cl)(η³:η³-C₁₀H₁₆), **4a.** The molecular precursor complex Pt(PEt₃)(Cl)(μ₂-Cl)₂Ru(Cl)(η³:η³-C₁₀H₁₆) was prepared using a modification of procedures reported for the synthesis of analogous complexes.¹⁶ A solution of 0.125 g (0.163 mmol) of Pt₂Cl₂(μ₂-Cl)₂(PEt₃)₂ and 0.10 g (0.163 mmol) of Ru₂Cl₂(μ₂-Cl)₂(C₁₀H₁₆)₂ in 15 mL of CH₂Cl₂ was stirred at room temperature for 20 min under a N₂ atmosphere. After this time, 40 mL of hexane was added to the reaction solution, and the solution was concentrated to ca. 10 mL at reduced pressure to give 0.190 g of **4a** (84% yield, mp 144–146 °C) as a brown powder. Complex **4a** can be crystallized from acetone/hexane solution. ¹H NMR [300 MHz, CDCl₃]: δ 1.24 (d of t, PCH₂CH₃, 9H), 1.86 (d of q, PCH₂, 6H), 2.33 (s, CH₂CHC(CH₃)CH₂, 3H), 2.35 (s, CH₂CHC(CH₃)CH₂, 3H), 2.40 (m, CH₂CHC(CH₃)CH₂, 2H), 2.5–2.8 (m, CH₂CHC(CH₃)CH₂, 2H), 4.53 (m, CH₂CHC(CH₃)CH₂, 1H), 4.97 (2s, CH₂CHC(CH₃)CH₂, CH₂CHC(CH₃)CH₂, 2H), 5.35 (s, CH₂CHC(CH₃)CH₂, 1H), 5.54 (s, CH₂CHC(CH₃)CH₂, 1H), 6.01 (s, CH₂CHC(CH₃)CH₂, 1H). ¹³C NMR [75 MHz, CDCl₃]: δ 7.58 (d, PCH₂CH₃, ²J_{PC} = 3.2 Hz), 14.2 (d, PCH₂, ¹J_{PC} = 40.5 Hz),

19.8 and 20.4 (CH₂CHC(CH₃)CH₂), 34.1 and 34.9 (CH₂CHC(CH₃)CH₂), 83.2 and 85.5 (CH₂CHC(CH₃)CH₂), 93.9 and 94.1 (CH₂CHC(CH₃)CH₂), 124.7 and 126.9 (CH₂CHC(CH₃)CH₂). ³¹P NMR [121 MHz, CDCl₃]: δ 8.39 (¹J_{PP} = 3784 Hz). Anal. Calcd for C₁₆H₃₁Cl₄PPtRu: C, 27.76; H, 4.51; P, 4.47. Found: C, 27.55; H, 4.64; P, 4.37.

Preparation of [(2,2'-Bipyridine)₂Ru(μ-2,2'-bipyrimidine)-PtCl₂][PF₆]₂, **5a.** The synthesis of [(bpy)₂Ru(μ-bpm)PtCl₂][PF₆]₂ was performed using a modification of a method reported for the synthesis of the ClO₄[−] salt of this compound.¹⁵ A solution of 0.640 g (1.52 mmol) of (DMSO)₂PtCl₂ and 1.084 g (1.26 mmol) of [Ru(bpy)₂(bpm)][PF₆]₂ in 50 mL of deoxygenated methanol was heated at reflux in darkness under a N₂ atmosphere for ca. 16 h. After the solution was cooled, a precipitate formed, which was collected by vacuum filtration, washed with diethyl ether, and dried under reduced pressure near room temperature for 4 h to give 1.362 g of **5a** as a brick-red solid (1.21 mmol, 96% yield). Anal. Calcd for C₂₈H₂₂N₈P₂F₁₂Cl₂-RuPt: C, 29.83; H, 1.97; N, 9.93. Found: C, 29.77; H, 2.02; N, 9.85.

General Procedure for the Preparation of Pt–Ru/Carbon Nanocomposites. Nanocomposites **1b**, **2b**, **3b**, **3c**, **4b**, and **5b** were prepared by appropriate thermal treatment of the corresponding single-source precursor/Vulcan carbon powder composites. Precursor complexes were deposited onto the carbon powder support by absorption/deposition from the solution phase, using either a single or multistep deposition procedure.^{5–7} For multistep depositions, equal masses of precursor were used for each deposition cycle with repetition of an initial thermal treatment procedure. All thermal treatments were performed in Lindberg tube furnaces that were equipped with quartz tubes. High-surface-area carbon (Vulcan XC72R) was purchased from Cabot Corporation. Combax alumina–silicate combustion boats, which were used as sample containers for all the nanocomposite syntheses, were purchased from Fisher Scientific. Flow rates of gaseous reactants were 150 mL/min. When changing the gaseous atmosphere from air to H₂/N₂ during heating protocols, an intermediate flush with nitrogen gas for 10 min at the appropriate reaction temperature was implemented as a safety feature. Heating rates for all the nanocomposite syntheses were 15 °C/min, except for nanocomposite **2b**, where the heating rate was 30 °C/min. Specific details on nanocomposite preparations, including characterization data for each nanocomposite, are provided in Table 1.

Direct Methanol Fuel Cell (DMFC) Performance Evaluation. DMFC testing results were obtained, using a 4-cm² test fixture that was equipped with a hydrogen reference electrode on the anode side of the membrane. The reference electrode consists of a small platinum gas-diffusion electrode located adjacent to (but electrically isolated from) the working anode and supplied with a flow of humidified hydrogen. Both anode and cathode potentials were measured with respect to this electrode, with the cell potential being the sum of the two. Experimental conditions used for these performance evaluations were the following: anode catalyst and loading, nanocomposites **3c**, **5b**, and Pt–Ru(1:1)/Vulcan carbon (obtained commercially from E-TEK, Inc.), 2 mg/cm² based on precious metal; cathode catalyst and loading, platinum black, 4 mg/cm² based on precious metal; membrane, Nafion 112; oxygen flow rate, 600 mL/min; oxygen backpressure, 30 psig; methanol flow rate, 2 mL/min; methanol backpressure, 30 psig; cell temperature, 80 °C. Electrocatalyst layers were deposited directly onto the Nafion 112 membrane, using standard ink electrode technology. Catalyst loadings of 2 mg/cm² of electrode surface (precious

TABLE 1: Preparation and Characterization Data for the Pt–Ru/Carbon Nanocomposites 1b–5b

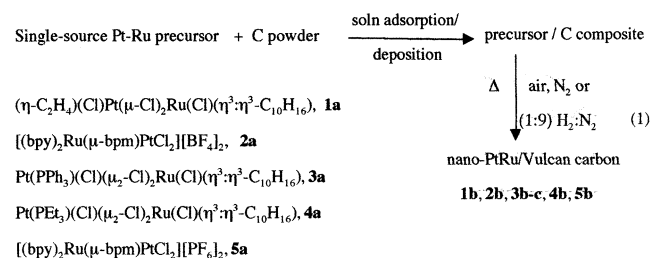
	1b	2b	3b	3c	4b	5b
precursor used	1a	2a	3a	3a	4a	5a
precursor mass (mg)	324	530	76	238	213	560
support mass (mg)	164	156	235	175	212	311
number of deposition cycles	3	1	1	2	2	2
cycle, T_1 – T_2 (°C) ^{a,b}	25–350 (H ₂ /N ₂)	25–650 (N ₂)	25–280 (air), 280–650 (H ₂ /N ₂)	25–350 (air), 350–650 (H ₂ /N ₂)	25–325 (air), 325–650 (H ₂ /N ₂)	25–280 (air), 280–650 (H ₂ /N ₂)
anneal conditions T (°C), t (h) ^b	350, 0.25 (N ₂)	650, 0.3 (H ₂ /N ₂)	650, 2.5 (N ₂)	650, 1.4 (N ₂)	650, 1.25 (N ₂)	650, 1 (N ₂)
wt % Pt (bulk)	22.28	20.08	4.43	15.90	18.00	16.20
wt % Ru (bulk)	12.88	8.20	2.70	9.84	9.42	8.83
wt % total metal (bulk)	35.16	28.28	7.13	25.74	27.42	25.03
Pt:Ru at. ratio (bulk)	0.89	1.27	0.85	0.84	0.99	0.95
Pt:Ru at. ratio (EDS)	1.27	0.90	0.92	1.04	1.22	1.38
average diameter, by TEM (nm)	2.6	4.3	3.6	4.0	5.7	44 (Pc) ^c
average diameter, by XRD (nm)	4.6 (fcc) ^c	4.2 (fcc) ^c	1.5 (fcc) ^c	^d	^d	^d

^a T_1 is the initial temperature, and T_2 is the final temperature. ^b Gas used is given in parentheses. H₂/N₂ = 1:9 H₂:N₂ (getter gas). ^c Abbreviations: fcc, face-centered cubic Pt–Ru phase; Pc, primitive-cubic PtRuP₂ phase. ^d Peak overlap of the fcc and Pc phases precludes an accurate determination of average particle size from direct measurement of XRD peak widths without curve convolution.

metal loading) were applied to the Nafion membrane, using a brushing technique. Following deposition of the ink, the catalyst layer was cured by hot pressing at ~200 °C for 45 s at a pressure of 400 psi. The membrane and electrode assembly was mounted in the test apparatus and evaluated. Performance curves were recorded at four different concentrations of methanol as the anode fuel, with data shown for a methanol concentration of 2 M.

Results and Discussion

Adsorption of the (1:1)-Pt,Ru dinuclear complexes **1a–5a** from the solution phase onto Vulcan carbon powder, followed by removal of residual solvent at reduced pressure, affords precursor/carbon composites as dry, black powders, as shown below in eq 1. Thermal treatment under reactive and/or inert



gaseous environments leads to degradation of the precursor complex with the loss of the nonmetallic elements and formation of Pt–Ru/Vulcan carbon powder nanocomposites (**1b–5b**). A summary of the preparation details and characterization data for each nanocomposite is provided in Table 1. The total metal content of each nanocomposite ranges from 7.13 wt % for nanocomposite **1b**, depending on the precursor/support mass ratio used in the preparation. For nanocomposites **1b**, **3c**, **4b**, and **5b**, a multistep protocol for precursor deposition was used to ensure a high dispersion of metal nanoparticles at the higher metal loading used for these nanocomposite preparations.

Although precursor decomposition reactions have not been studied in detail for each precursor used in this study, the reactive degradation of precursor **1a** in a 1:9 H₂:N₂ (getter gas) atmosphere has been studied by thermogravimetric analysis and by bulk product analysis.¹⁷ Under these reducing conditions, complex **1a** undergoes a rapid loss of the bis-allyl, ethylene, and two chloro ligands by 90 °C and the loss of the remaining chloro ligands by 120 °C, giving a residual mass content of

50.4 wt %, which is almost consistent with a theoretical Pt–Ru metal content of 49.2 wt %.¹⁷ The products of this reductive degradation are 2,7-dimethyloctane and HCl, representing reductive elimination of the chloro ligands as HCl and complete hydrogenation of the bis-allyl ligand. Mass losses recorded during nanocomposite syntheses indicate substantial elimination of the nonmetallic elements of each precursor used in this study. Although retention of residual amounts of nonmetallic elements is not uncommon in precursor-decomposition syntheses, the formation of a ternary metal phosphide phase when using precursors containing phosphorus was unexpected, as discussed below. TGA analysis of the degradation of the phosphorus-containing precursor **3a** supported on Vulcan carbon under either air or nitrogen is consistent with phosphorus retention. When the material is heated to 450 °C, mass loss occurs in two steps, centered at 178 and 332 °C, respectively. Mass loss at the lower temperature is consistent with complete elimination of the bis-allyl ligand, whereas the observed additional mass loss up to 350 °C is consistent with the loss of three phenyl groups. However, products resulting from these thermal degradation reactions have not been identified.

Precursors **1a** and **2a** lack phosphorus and form Pt–Ru/carbon nanocomposites **1b** and **2b**, respectively, as expected from analogous reactions.^{5,6} Representative BF TEM images, EDS spectra, and XRD scans of nanocomposites **1b** and **2b** are displayed in Figures 1 and 2, respectively. TEM micrographs reveal metal particles of high contrast, widely dispersed on the carbon support, having average diameters of 2.6 or 4.3 nm, respectively. Broad-area EDS spectra show emission from platinum and ruthenium, with relative intensities corresponding to Pt/Ru atomic ratios of 1.27 and 0.90, respectively, on the micrometer scale. Cu X-ray emission from the TEM holey carbon/copper grids is also observed.

XRD scans of nanocomposites **1b** and **2b** reveal amorphous scattering from the carbon powder support at ~25° 2 θ and a predominant, face-centered-cubic (fcc) pattern of peaks consistent with that expected for Pt–Ru alloys with cell constants of 3.87 ± 0.02 Å.¹⁸ Peaks associated with this alloy phase are identified by the appropriate Miller indices. Scherrer's analysis of experimentally measured XRD peak widths for nanocomposites **1b** and **2b** gives average crystalline domain sizes of 4.6 and 4.2 nm, respectively, for the alloy nanoparticles.¹⁴ Diffraction peaks near 38° and 44° in 2 θ from ruthenium metal are not observed; thus, any metal phase separation that might have occurred during synthesis is not evident by direct inspection. In addition, an SAD ring pattern obtained from nanocomposite

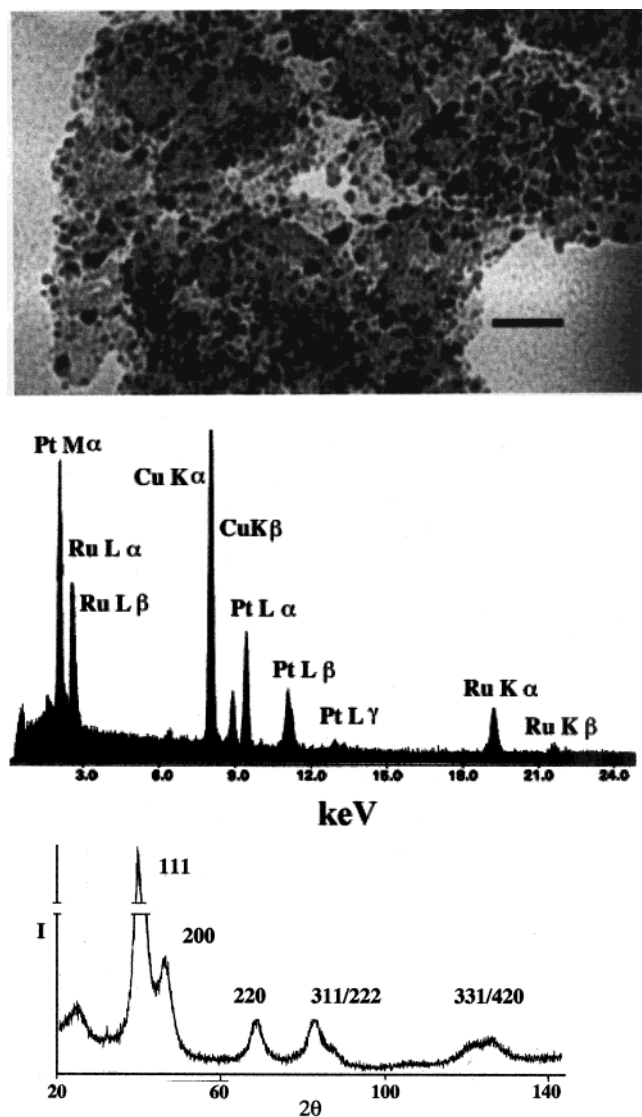


Figure 1. Bright-field TEM image (top), EDS spectrum (middle), and powder XRD scan (bottom) of the Pt–Ru/carbon nanocomposite **1b**.

1b reveals five rings, the *d*-spacings of which are appropriate for the (111), (200), (220), (311), and (331/420) planes of the Pt–Ru fcc unit cell.

To investigate the compositional integrity of nanocrystals prepared using this synthesis strategy, the Pt/Ru atomic ratio of multiple, randomly chosen nanocrystals within nanocomposites **1b** and **2b** were measured experimentally by HR-EDS. The integrated intensities of the Pt $L\alpha_1$ and Ru $K\alpha_{1,2}$ emissions from individual alloy nanoclusters were collected using a field-emission gun (FEG) with a spot size of 1.4 nm and were converted to Pt/Ru atomic ratios as previously described.⁵ Plots of Pt/Ru atomic ratios versus nanocluster size for nanocrystals within nanocomposites **1b** and **2b** are shown in Figure 3. Error bars for the Pt/Ru atomic ratios are calculated from error propagation and are based principally on EDS counting statistics. The particle size distribution of those metal nanoclusters randomly chosen for on-particle HR-EDS measurements is essentially identical to that determined from TEM micrographs.

In regard to compositional variation on the nanocluster scale, only statistical arguments can be made. HR-EDS measurements indicate the absence of detectable amounts of platinum or ruthenium in regions of the carbon support not containing nanoparticles; thus, the metal content of these samples seems to be localized primarily within observable nanoparticles.

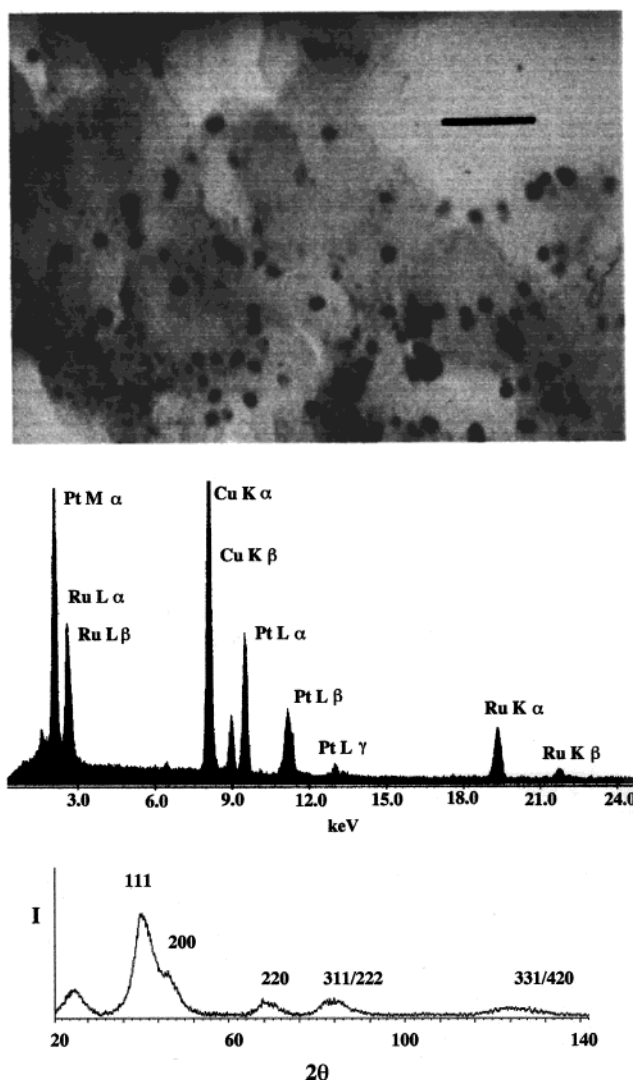


Figure 2. Bright-field TEM image (top), EDS spectrum (middle), and powder XRD scan (bottom) of the Pt–Ru/carbon nanocomposite **2b**.

Average Pt/Ru stoichiometries for nanoclusters within nanocomposites **1b** and **2b** are 0.92 (19) and 1.26 (15), respectively, where the standard deviations given (in parentheses) are weighted for the experimental uncertainty associated with each on-particle measurement. This error is principally due to experimental uncertainties associated with the HR-EDS counting statistics but also includes particle-to-particle variations in metal stoichiometry. These Pt/Ru stoichiometries are within one standard deviation of those determined by bulk elemental microanalysis and within 1.5 standard deviations of the 1:1 Pt/Ru stoichiometries of the precursor complexes. Gross phase separation of the two metals is not evident on the nanoscale.

In contrast, characterization data for metal alloy/carbon nanocomposites prepared using precursors **3a**, **4a**, or **5a** give unexpected results. Each of these precursors contains phosphorus, either as a phosphine ligand (**3a** and **4a**) or within a counterion (**5a**). Knowing that thermal degradation of ruthenium or platinum phosphine complexes under solely reducing conditions respectively produces the binary-metal phosphide phases RuP and PtP₂,¹⁹ Vulcan carbon composites of these precursors were subjected to initial air oxidation in an attempt to separate phosphorus from the metal-alloy phase. Mild oxidation treatments are employed, however, to minimize ruthenium loss through the possible formation of volatile metal oxides.

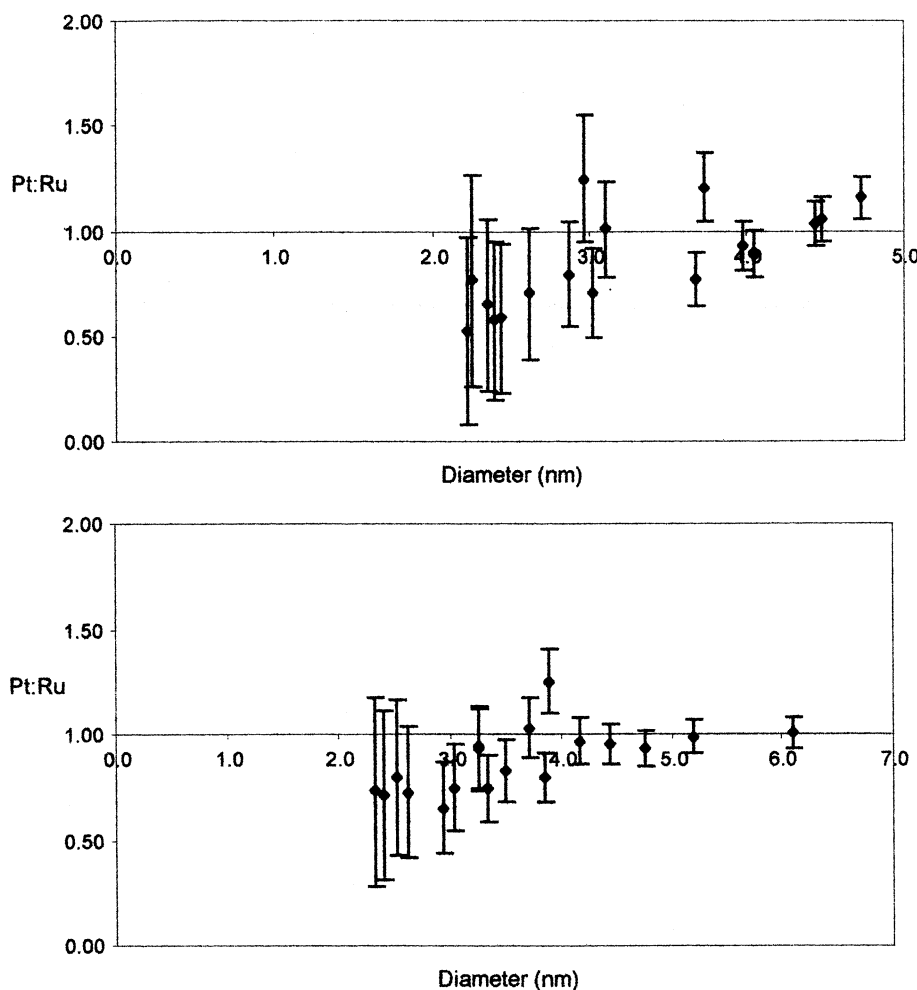


Figure 3. Pt:Ru atomic ratios of individual nanocrystals versus nanocrystal diameter, as determined by HRTEM FEG EDS for nanocomposites **1b** (top) and **2b** (bottom).

Thermal degradation of precursor **3a**/Vulcan carbon composites at two different loadings gives nanocomposites **3b** and **3c**, with total metal contents of 7.13 and 25.74 wt %, respectively. Representative characterization data for nanocomposite **3b** are shown in Figure 4. TEM micrographs reveal metal particles of high contrast, with an average diameter of 3.6 nm, widely dispersed on the carbon support. A broad-area EDS spectrum shows emission from Pt and Ru, with relative intensities corresponding to a Pt/Ru atomic ratio of 0.92, in addition to Cu X-ray emission from the TEM grids used. XRD scans of nanocomposite **3b** reveal amorphous scattering from the carbon powder support at $\sim 25^\circ 2\theta$ and a fcc pattern of peaks consistent with that expected for Pt–Ru alloys (as identified by the appropriate Miller indices). Scherrer's analysis of experimentally measured XRD peak widths for this fcc phase gives an average crystalline domain size of only 1.5 nm for the alloy nanoparticles. Small metal particles are usually formed at low precursor loading, because less metal is deposited on the surface of the carbon support. However, two comparatively sharp diffraction peaks, located near 32° and $46^\circ 2\theta$, are also present. These peaks, designated by an "X" in Figure 4, do not correspond to the principal diffraction peaks of ruthenium metal or of any known binary-metal phosphide composition of platinum or ruthenium.

However, XRD scans of nanocomposites **3c**, **4b**, and **5b**, which were prepared using high loadings of precursors **3a**, **4a**, or **5a**, respectively, all display the same two unassigned diffraction peaks observed with nanocomposite **3b** but with

much greater relative intensity (see Figure 5). These three nanocomposites have relatively high total-metal compositions of 25–27 wt %. Analysis of the observed diffraction peak positions reveals two overlapping XRD patterns. One pattern is identical to that expected, and previously observed, for a fcc Pt–Ru alloy phase (peaks denoted as "F" in Figure 5). The second pattern is consistent with a primitive cubic phase (peaks denoted as "P" in Figure 5). These two patterns account for all the diffraction peaks observed for these nanocomposites, excluding the amorphous scattering peak of the carbon support near $25^\circ 2\theta$. Given the suspicion that the primitive-cubic phase might contain phosphorus, nanocomposite **4b** was analyzed for both metal and phosphorus content by commercial elemental microanalysis. This nanocomposite contains 2.52 wt % phosphorus, giving an empirical formula of $\text{Pt}_1\text{Ru}_1\text{P}_{0.9}$, which is quite consistent with the elemental stoichiometry of precursor **4a**.

Although this unknown phase cannot be isolated as a pure material, an XRD scan of this phase suitable for Rietveld analysis can be obtained by adding additional phosphorus to the precursor/carbon composite prior to thermal treatment. In work that has been described elsewhere, chemical evidence and full-profile Rietveld analysis of this XRD pattern identifies this substance as a ternary, interstitial metal phosphide that has the composition PtRuP_2 at maximum phosphorus incorporation.²⁰ The structure of this substance can be represented equivalently either as a primitive-cubic unit cell with a cell constant of 2.78 Å with Pt and Ru atoms randomly disordered at the corners of the cubic cell and a single P atom located at the cell center, or

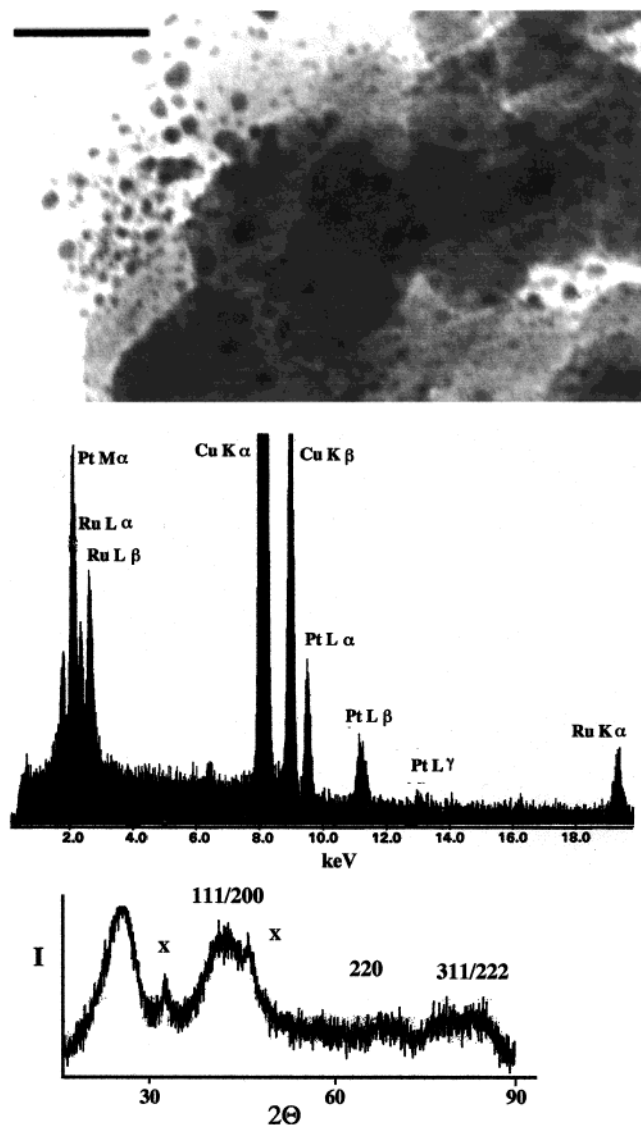


Figure 4. Bright-field TEM image (top), EDS spectrum (middle), and powder XRD scan (bottom) of the Pt–Ru/carbon nanocomposite **3b**. Diffraction peaks denoted as “X” represent diffraction from an unexpected phase.

as a fcc unit cell ($Fm\bar{3}m$) with a cell constant of 5.56 Å with randomly disordered Pt and Ru atoms located at the (0,0,0) and $(\frac{1}{2}, \frac{1}{2}, \frac{1}{2})$ atomic positions and P atoms located at the $(\frac{1}{4}, \frac{1}{4}, \frac{1}{4})$ positions. This structure is atypical for metal phosphides of stoichiometries MP or $MM'P_2$ ²¹ but represents interstitial placement of a P atom within a cubic array of randomized metal atoms. In $PtRuP_2$, the M–M distance of 2.78 Å gives overall expansion of the unit cell parameter by only 1.5%, relative to the fcc unit cell of the observed Pt–Ru alloy phase.

Assuming that all of the phosphorus in nanocomposite **4b** is present as $PtRuP_2$, the overall composition of this material is then $(PtRu)_{0.55}(PtRuP_2)_{0.45}$. Such a mixed-phase composition is consistent with the overlapping fcc and primitive-cubic XRD patterns shown in Figure 5.

Previous results confirm that Pt–Ru/Vulcan carbon nanocomposites prepared using precursor **1a** and thermal treatment protocols similar to those used in the preparation of nanocomposites **3b–5b** exhibit high performance as DMFC anode catalysts, relative to that measured for commercial Pt–Ru/C electrocatalysts.⁵ Knowing that interstitial inclusion of phosphorus into the Pt–Ru alloy structure occurs with only a slight change in M–M distance, an interesting question arises: Will

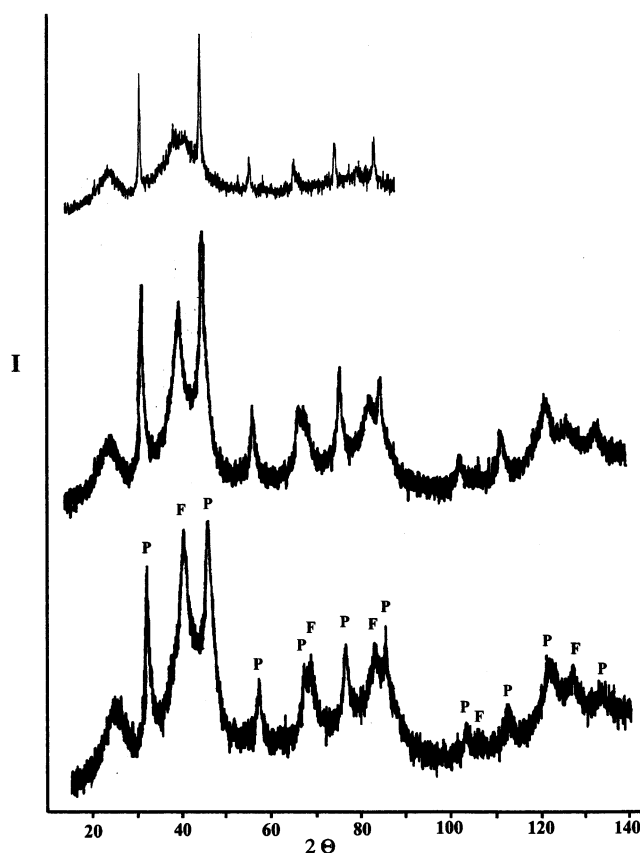


Figure 5. Powder XRD scans of the Pt–Ru/carbon nanocomposites **3c** (bottom), **4b** (middle), and **5b** (top).

nanocomposites containing the $PtRuP_2$ phase, such as nanocomposites **3b–5b**, perform poorly, relative to commercial Pt–Ru/C electrocatalysts, because of a “poisoning” effect of the P atoms? To answer this question, we measured the performance of nanocomposites **3c** and **5b** as DMFC anode catalysts, relative to the performance of a commercial Pt–Ru/C electrocatalyst. Current–voltage curves of the anode electrode in DMFCs fabricated using nanocomposites **3c**, **5b**, or a (1:1) Pt–Ru/C catalyst (obtained from E-TEK, Inc.) as anode catalysts are shown in Figure 6. For each test, the anode catalyst loading is 2 mg of precious metal/cm². The anode potential was measured with respect to the hydrogen reference electrode. All data were collected with current that was held constant for 30 s before recording the potential. Membrane electrode assembly (MEA) fabrication and cell performance measurements were performed using a common experimental protocol.

Although considerable care must be taken when interpreting relative catalytic performance, because of the many variables present within the experiment, we were surprised to observe that all three nanocomposites tested with similar performance. Both the anode and overall DMFC cell performances measured for nanocomposite **5b** essentially overlap with the performance recorded for the commercial supported catalyst. Nanocomposite **3c** actually performs slightly higher than the commercial catalysts at all current densities, although this enhancement might not be highly significant. At a current density of 400 mA/cm², nanocomposite **3c** outperforms the commercial catalyst by ca. 55 mV. It is apparent that the presence of substantial amounts of $PtRuP_2$ does not poison the catalytic performance of these nanocomposites and might even slightly enhance methanol electrooxidation. This result was not anticipated, because other main-group elements, such as sulfur, act as effective poisons for Pt–Ru DMFC anode electrocatalysis.⁸ Synthesis strategies

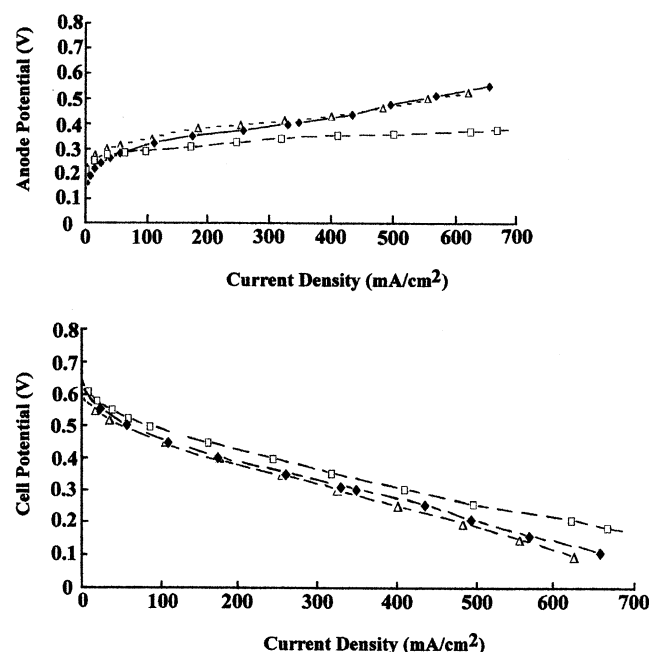


Figure 6. DMFC anode (top) and cell (bottom) current density–voltage (V) curves, comparing the performance of nanocomposites (□) **3c** and (◆) **5b** to that of (Δ) a commercial supported Pt–Ru colloid at an anode catalyst loading of 2 mg of total metal/cm². The anode potential was measured with respect to the hydrogen reference electrode. All data were collected with current that was held constant for 30 s before recording the potential.

suitable for the preparation of significant amounts of PtRuP₂ as a pure substance need to be discovered, so that the electrocatalytic reactivity of this ternary phase can be directly interrogated. At present, only samples containing both Pt–Ru alloy and PtRuP₂ phases are available for electrochemical testing.

We speculate that the interstitial location of the P atoms in PtRuP₂ mitigates any poisoning influence of phosphorus. Given that phosphorus is more electronegative than heavy transition-metal atoms, the surface metal atoms of PtRuP₂ nanocrystals should be slightly more electron-deficient than surface atoms in Pt–Ru alloy nanocrystals. We suggest that interstitial ternary phases of the general composition Pt_xRu_yE_z (where E represents a main-group heteroelement) might permit compositional tuning of the electrocatalytic reactivity of such ternary alloys. Synthesis strategies designed for the targeted preparation of such materials need to be developed, along with a better understanding of the chemical stability and catalytic reactivity of such materials within a working fuel cell environment. In support of this speculation, it is interesting to note that Mo–Ru–E (where E = S or Se) ternary alloys serve as methanol-tolerant electrocatalysts for oxygen reduction, even though sulfur and selenium normally poison electrocatalytic reactivity.^{22,23}

Acknowledgment. Research support provided by the U.S. Army Research Office, under Grant Nos. DAAH04-95-1-0146, DAAH04-96-1-0179, DAAH04-96-1-0302, and DAAG55-98-1-0362, is gratefully acknowledged by C.M.L. On-particle EDS and HR-TEM measurements performed at the Oak Ridge National Laboratory SHaRE Collaborative Research Center was sponsored by the Division of Materials Sciences and Engineering, U.S. Department of Energy, under Contract No. DE-AC05-00OR22725 with UT-Battelle, LLC.

References and Notes

- (1) (a) Hogarth, M. P.; Ralph, T. R. *Platinum Met. Rev.* **2002**, *46*, 146. (b) Ralph, T. R.; Hogarth, M. P. *Platinum Met. Rev.* **2002**, *46*, 117. (c) Hamnett, A. *Catal. Today* **1997**, *38*, 445. (d) Hogarth, M. P.; Hards, G. A. *Platinum Met. Rev.* **1996**, *40*, 150. (e) Chandler, G. K.; Genders, J. D.; Pletcher, D. *Platinum Met. Rev.* **1997**, *41*, 54. (f) Ralph, T. R. *Platinum Met. Rev.* **1997**, *41*, 102. (g) Hamnett, A.; Troughton, G. L. *Chem. Ind.* **1992**, 480. (h) Ren, X.; Wilson, M. S.; Gottesfeld, S. *J. Electrochem. Soc.* **1996**, *143*, L12. (i) Hogarth, M. P.; Christensen, P. A.; Hamnett, A. In *New Materials for Fuel Cell Systems I*, Proceedings of the 1st International Symposium on New Materials for Fuel Cell Systems, Montreal, July 9–13, 1995; 310. (j) Lin, W. F.; Wang, J. T.; Savinell, R. F. *J. Electrochem. Soc.* **1997**, *144*, 1917. (k) Gasteiger, H. A.; Markovic, N.; Ross, P. N., Jr.; Cairns, E. J. *J. Electrochem. Soc.* **1994**, *141*, 1795. (l) Surampudi, S.; Narayanan, S. R.; Vamos, E.; Frank, H.; Halpert, G.; LaConti, A.; Kosek, J.; Surya Prakash, G. K.; Olah, G. A. *J. Power Sources* **1994**, *47*, 377. (m) Wang, K.; Gasteiger, H. A.; Markovic, N. M.; Ross, P. N., Jr. *Electrochim. Acta* **1996**, *41*, 2587. (n) Pathanjali, G. A.; Krishnamurthy, B.; Chireau, R. F.; Mital, C. K. *Bull. Electrochem.* **1996**, *12*, 193.
- (2) (a) Reddington, E.; Sapienza, A.; Gurau, B.; Viswanathan, R.; Sarangapani, S.; Smotkin, E. S.; Mallouk, T. E. *Science* **1998**, *280*, 1735. (b) Gurau, B.; Viswanathan, R.; Liu, R.; Lafrenz, T.; Lye, K. L.; Smotkin, E. S.; Reddington, E.; Sapienza, A.; Chan, B. C.; Mallouk, T. E.; Sarabgapani, S. *J. Phys. Chem. B* **1998**, *102*, 9997. (c) Gotz, M.; Wendt, H. *Electrochim. Acta* **1998**, *43*, 3637.
- (3) (a) Watanabe, M.; Uchida, M.; Motoo, S. *J. Electroanal. Chem.* **1987**, *229*, 395. (b) Nashner, M. S.; Frenkel, A. I.; Adler, D. L.; Shapley, J. R.; Nuzzo, R. G. *J. Am. Chem. Soc.* **1997**, *119*, 7760. (c) Nashner, M. S.; Frenkel, A. I.; Somerville, D.; Hills, C. W.; Shapley, J. R.; Nuzzo, R. G. *J. Am. Chem. Soc.* **1998**, *120*, 8093. (d) Hills, C. W.; Nashner, M. S.; Frenkel, A. I.; Shapley, J. R.; Nuzzo, R. G. *Langmuir* **1999**, *15*, 690. (e) Pan, C.; Dassenoy, F.; Casanove, M. J.; Philippot, K.; Amiens, C.; Lecante, P.; Mosset, A.; Chaudret, B. *J. Phys. Chem. B* **1999**, *103*, 10098. (f) Tess, M. E.; Hill, P. L.; Torracca, K. E.; Kerr, M. E.; Addoud, K. A.; McElwee-White, L. *Inorg. Chem.* **2000**, *39*, 3942. (g) Liu, L.; Pu, C.; Viswanathan, R.; Fan, Q.; Liu, R.; Smotkin, E. S. *Electrochim. Acta* **1998**, *43*, 3657. (h) Arico, A. S.; Creti, P.; Modica, E.; Monforte, G.; Baglio, V.; Antonucci, V. *Electrochim. Acta* **2000**, *45*, 4319.
- (4) Arico, A. S.; Shukla, A. K.; El-Khatib, K. M.; Creti, P.; Antonucci, V. *J. Appl. Electrochem.* **1999**, *29*, 671.
- (5) Boxall, D. L.; Deluga, G. A.; Kenik, E. A.; King, W. D.; Lukehart, C. M. *Chem. Mater.* **2001**, *13*, 891.
- (6) (a) Steigerwalt, E. S.; Deluga, G. A.; Cliffel, D. E.; Lukehart, C. M. *J. Phys. Chem. B* **2001**, *105*, 8097. (b) Steigerwalt, E. S.; Deluga, G. A.; Lukehart, C. M. *J. Phys. Chem. B* **2002**, *106*, 760.
- (7) (a) Lukehart, C. M.; Boxall, D. L.; Corn, J. D.; Hariharasarma, M.; King, W. D.; Kwiatkowski, K. C.; Steigerwalt, E. S.; Kenik, E. A. *Prepr. Symp.—Am. Chem. Soc., Div. Fuel Chem.* **1999**, *44*, (4), 982. (b) Boxall, D. L.; Lukehart, C. M.; Kenik, E. A. *AES (Am. Soc. Mech. Eng.)* **1999**, *39*, 327. (c) Boxall, D. L.; Kenik, E. A.; Lukehart, C. M. *Mater. Res. Soc. Symp. Proc.* **2001**, *589*, 265. (d) Lukehart, C. M. U.S. Patent 6,232,264, May 15, 2001.
- (8) Chin, D.-T.; Howard, P. D. *J. Electrochem. Soc.* **1986**, *133*, 2447.
- (9) Smithies, A. C.; Schmidt, P.; Orchin, M. *Inorg. Synth.* **1970**, *12*, 240.
- (10) Goodfellow, R. J.; Venanzi, L. M. *J. Chem. Soc.* **1965**, 7533.
- (11) Price, J. H.; Williamson, A. N.; Schramm, R. F.; Wayland, B. B. *Inorg. Chem.* **1972**, *11*, 1280.
- (12) Cox, D. N.; Roulet, R. *Inorg. Chem.* **1990**, *29*, 1360.
- (13) Nallas, G. N. A.; Jones, S. W.; Brewer, K. J. *Inorg. Chem.* **1996**, *35*, 6974.
- (14) Klug, H. P.; Alexander, L. E. *X-ray Diffraction Procedures for Polycrystalline and Amorphous Materials*, Second Edition; Wiley: New York, 1974.
- (15) Sahai, R.; Rillema, D. P. *Inorg. Chim. Acta* **1986**, *118*, L35.
- (16) Severin, K.; Polborn, K.; Beck, W. *Inorg. Chim. Acta* **1995**, *240*, 339.
- (17) Steigerwalt, E. S.; Deluga, G. A.; Lukehart, C. M. *J. Phys. Chem. B* **2002**, *106*, 760.
- (18) Radmilovic, V.; Gasteiger, H. A.; Ross, P. N., Jr. *J. Catal.* **1995**, *154*, 98.
- (19) Lukehart, C. M.; Milne, S. B.; Stock, S. R. *Chem. Mater.* **1998**, *10*, 903.
- (20) Kwiatkowski, K. C., Ph.D. Thesis, Vanderbilt University, Nashville, TN, 2000.
- (21) von Schnering, H. G.; Honle, W. *Encyclopedia of Inorganic Chemistry*; John Wiley and Sons: Chichester, U.K., 1994; Vol. 6, p 3106.
- (22) Solorza-Feria, O.; Ellmer, K.; Giersig, M.; Alonso-Vante, N. *Electrochim. Acta* **1994**, *39*, 1647.
- (23) Reeve, R. W.; Christensen, P. A.; Hamnett, A.; Haydock, S. A.; Roy, S. C. *J. Electrochem. Soc.* **1998**, *145*, 3463.